Pseudohalide-Exchanged Quantum Dot Solids Achieve Record Quantum Efficiency in Infrared Photovoltaics

*Bin Sun, Oleksandr Voznyy, Hairen Tan, Philipp Stadler, Mengxia Liu, Grant Walters, Andrew H. Proppe, Min Liu, James Fan, Taotao Zhuang, Jie Li, Mingyang Wei, Jixian Xu, Younghoon Kim, Sjoerd Hoogland, and Edward H. Sargent**

Application of pseudohalogens in colloidal quantum dot (CQD) solar-cell active layers increases the solar-cell performance by reducing the trap densities and implementing thick CQD films. Pseudohalogens are polyatomic analogs of halogens, whose chemistry allows them to substitute halogen atoms by strong chemical interactions with the CQD surfaces. The pseudohalide thiocyanate anion is used to achieve a hybrid surface passivation. A fourfold reduced trap state density than in a control is observed by using a suite of field-effect transistor studies. This translates directly into the thickest CQD active layer ever reported, enabled by enhanced transport lengths in this new class of materials, and leads to the highest external quantum efficiency, 80% at the excitonic peak, compared with previous reports of CQD solar cells.

Colloidal quantum dots (CQDs) are promising materials for solar cells: their bandgap is tunable via the quantum size effect, and they thereby enable broadband solar spectra utilization.[1–6] The recent achievement of solution-phase exchanges to final, production-compatible ink, has provided a new pathway for single-step, large-scale fabrication of CQD solar cells. Recently, rapid progress has been made in both surface chemistry and device architectures, contributing to certified power conversion efficiencies (PCE) that recently reached 11.3%.[7–12]

A thick CQD absorber layer is a prerequisite to achieve high photocurrent density and thus high PCE in solar cells.[13,14] However, the transport of photoexcited carriers throughout the complete length of such CQD films is limited by trapping.[8] As-prepared PbX (X = S, Se) CQDs are off-stoichiometric and lead-rich,[15] conditions that lead to mid-gap trap states.[16] In the latest record-performing devices, improvements have arisen mainly from judicious management of the CQD surface stoichiometry. Halide anions (Cl^-, Br^-, I^-)[12,17,18] and molecular halides (Cl_2, I_2)[11,19] have reduced trap states and enabled lower trap densities, leading directly to the improved PCE. Dangling Pb bonds responsible for sub-bandgap states[20] can also be reduced by passivating with strongly binding chalcogens.[21]

We took the view that the success of halides in chalcogenide quantum-dot passivation merited renewed explorations of the potential for pseudohalides (SCN^-, CN^-, N_3^-) to achieve similar or desirably even greater performance. The photocurrent density so far achieved using halides (below 28 mA cm^{-2}) stands to improve further.[11,12,22,23] There exist initial indicators that mixed-anionic-passivant strategies can outperform strategies that rely only on a single class of ligands.[21]

Pseudohalides as hybrid passivating agents offer strong chemical interaction with the CQD surfaces.[24–27] The thiocyanate anion, SCN^-, is an ambidentate linear ligand: it can bond to CQDs by both S- and N-bound coordination modes.[25,26] In principle, it therefore offers to act simultaneously as a crosslinker and a spacer in PbS solids. Indeed, an impressive electron mobility of 0.1 $cm^2\ V^{-1}\ s^{-1}$ has been reported for PbS nanocubes that employed a solid-state ligand exchange with SCN.[26]

Here, we devise a hybrid passivation approach that significantly reduced the trap density in CQD films. Our strategy combines halides and SCN ions during the solution-exchange. We obtained stable CQD inks and demonstrated record-thickness high-performing CQD films. This led to the highest external quantum efficiency (EQE) at the excitonic peak—an EQE of 80%—compared with previous reports of CQD solar cells. The record solar PCE devices based on PbS CQDs showed an EQE of 70% employing 350-nm-thick CQD films.[11,12,28]

Exchanged PbS CQDs (**Figure 1**) are capped by iodide ions and separated by SCN ions. For the control method (CTL), we used PbI_2 and ammonium acetate (AA) in *N*,*N*-dimethylformamide (DMF) as the precursor solution.[12] Oleic acid (OA)-capped CQDs transfer from the octane nonpolar phase into the DMF polar phase, leaving the long ligands OA in the nonpolar phase. After the ligand exchange, only $[I]^-$ remains on the

Dr. B. Sun, Dr. O. Voznyy, Dr. H. Tan, Prof. P. Stadler, M. Liu, G. Walters, A. H. Proppe, Dr. M. Liu, J. Fan, Dr. T. Zhuang, Dr. J. Li, M. Wei, J. Xu, Dr. Y. Kim, Dr. S. Hoogland, Prof. E. H. Sargent
Department of Electrical and Computer Engineering
University of Toronto
10 King's College Road, Toronto, Ontario M5S 3G4, Canada
E-mail: ted.sargent@utoronto.ca
Dr. P. Stadler
Institute of Physical Chemistry
Johannes Kepler University Linz
Altenbergerstr. 69, 4040 Linz, Austria
The ORCID identification number(s) for the author(s) of this article can be found under http://dx.doi.org/10.1002/adma.201700749.

DOI: 10.1002/adma.201700749

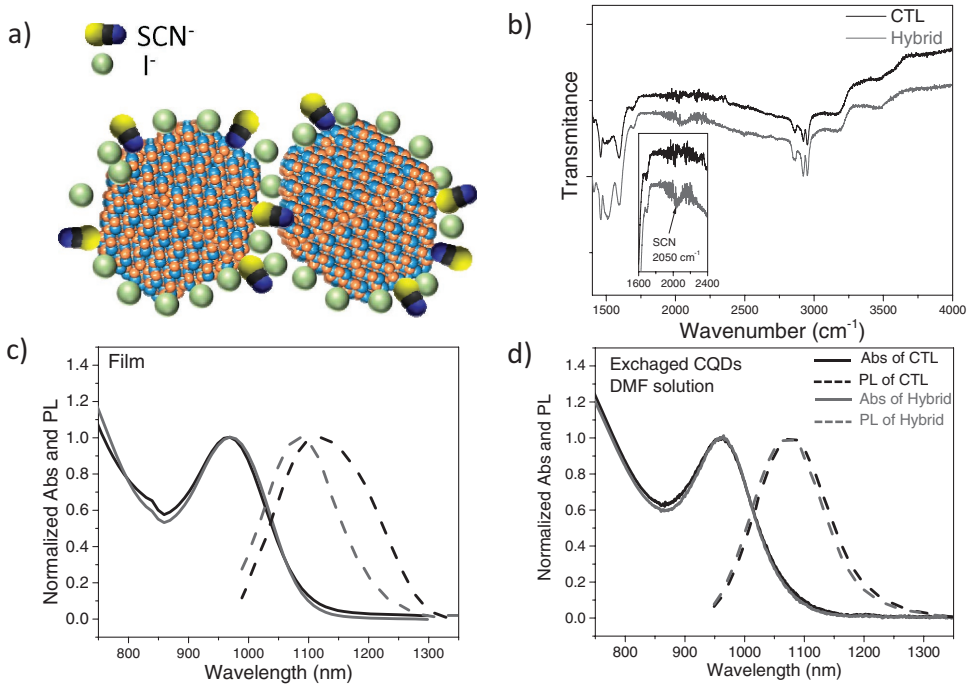

Figure 1. Schematic diagram of PbS CQD capped by I^- and SCN^- ions and photoelectrical properties. a) Hybrid ligand-exchanged CQDs separated by SCN anions. b) Attenuated total reflection Fourier transform infrared spectroscopy (ATR-FTIR) of CQD films on glass. Absorption and photoluminescence spectra of c) CQD films and d) CQDs in DMF solution with and without SCN additive.

surface of the CTL CQDs. When a small amount of $Pb(SCN)_2$ is added to the exchange precursor solution, the CQDs become capped by both $[I]^-$ and $[SCN]^-$. Figure 1b presents the infrared spectra of the CTL and hybrid films. The peak at 2050 cm^{-1}, which is ascribed to the thiocyanate stretching transition, indicates the presence of SCN ions following the hybrid treatment.

We also characterized the CQDs' spectral absorption (Abs) and photoluminescence (PL) in DMF solution, and also in CQD films, to compare hybrid passivation and simple iodide passivation (the latter as control, CTL). The Abs of CTL and hybrid CQD films (Figure 1c) show similar absorption features, their exciton peaks each positioned at 965 nm. However, the PL spectra are dramatically different. The PL peak position of the hybrid CQD film (1085 nm) reveals a smaller Stokes shift for the hybrid CQD film. Additionally, the PL full-width at half maximum of the hybrid CQD film is narrower than that of CTL CQD film (141 vs 192 nm). These initial indications suggested the potential for reduced bandtailing in the hybrid material compared to CTL.[29] The PL shift from solution to solid (35 nm) for CTL CQDs hints at heterogeneous aggregation and/or CQD fusion.

To study the mobility and trap state density of the exchanged CQD films, we carried out field-effect transistor (FET) measurements. Bottom-gate top-contact configurations (**Figure 2**a) were used to evaluate CQD film transport. 70 nm Ti and 10 nm ZrO_2 are deposited on glass, sequentially, as gate and the dielectric layer (Figure S1, Supporting Information, for details). Figure 2b shows the FET transfer characteristics in the linear region at a drain voltage of 100 mV. The carrier mobility is calculated from the slope of the I_{DS} versus V_{GS} plot according to the equation, $I_{DS} = \mu C_i \frac{W}{L}(V_{GS} - V_{TH})V_{DS}$, where μ is the carrier mobility in the linear regime; I_{DS} is the drain current; L and W are the channel length (50 μm) and channel width (2500 μm), respectively; C_i is the gate dielectric layer capacitance per unit area; V_{GS} and V_{TH} are the gate voltage and threshold voltage, respectively. The CTL and hybrid films have electron mobilities of 0.065 ± 0.003 and 0.061 ± 0.004 $cm^2\ V^{-1}\ s^{-1}$ (from at least 5 samples), respectively. The mobility of the hybrid films is slightly lower than the CTL films, a fact that may arise from a slightly increased interdot space when the SCN ion is present. We extracted the mobilities of CTL and hybrid films (Figure S2 (Supporting Information), values 0.070 ± 0.005 and 0.064 ± 0.002 $cm^2\ V^{-1}\ s^{-1}$) from the saturation regime, which are in good agreement with the mobilities extracted from the linear regime. We only observed n-type transport in the CTL and hybrid films, because in both films the main capping ligand is iodide.[30] When PbS nanocrystals are passivated by pure SCN, they will show ambipolar characteristics in FETs having the balanced hole and electron mobilities as high as ≈0.1 $cm^2\ V^{-1}\ s^{-1}$.[26]

We also retrieved the density of tail states from measured transfer characteristics.[31] The 10 nm of ZrO_2 provides a high gate capacitance of 700 nF cm^{-2}, large enough to shift the semiconductor active layer Fermi energy by several hundred millivolts. Varying the gate bias over a range of approximately few hundred millivolts allowed us to map the Fermi energy shift.[18,32] By analyzing the drain current's exponential increase below V_{TH}, which corresponds to in-gap transport through traps, we acquire information regarding in-gap trap states. The subthreshold region from V_{ON} to V_{TH} is used to calculate the density of in-gap trap states:[33]

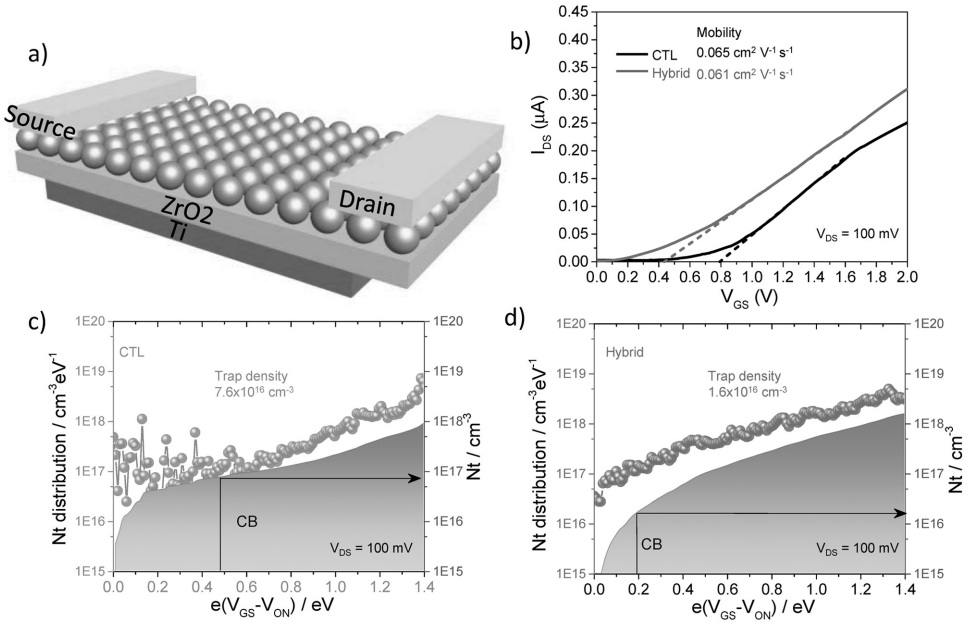

Figure 2. CQD solids mobility and traps determined by FET. a) Bottom-gate top-contact field-effect transistor structure. b) Transfer characteristics of CTL and hybrid CQD FETs. c,d) Trap state density (N_t) as a function of gate bias as calculated by Equation (1) for CTL (c) and hybrid CQD FETs (d).

$$N_t = \left[\left(\frac{Se}{kT\ln(10)} - 1\right)\frac{C_i}{e}\right]^2 \epsilon_0 \epsilon_r^{-1} \quad (1)$$

where S is a subthreshold swing, the slope of the gate voltage versus the log drain current below V_{TH} that defines the boundary between the substrate and transport regime; ϵ_0 is the vacuum permittivity; ϵ_r is the electric constant of the film, estimated to be 10.9.[24] In this way, we obtain the trap density of hybrid as $1.6 \pm 0.3 \times 10^{16}$ cm^{-3}, which is ≈4 times lower than that of CTL films ($7.6 \pm 0.8 \times 10^{16}$ cm^{-3}).

We sought then to investigate whether reduced trap density obtained via the hybrid treatment could lead to improved photovoltaic performance. To this end we fabricated CQD solar cells with the structure shown in **Figure 3**a. We first investigated

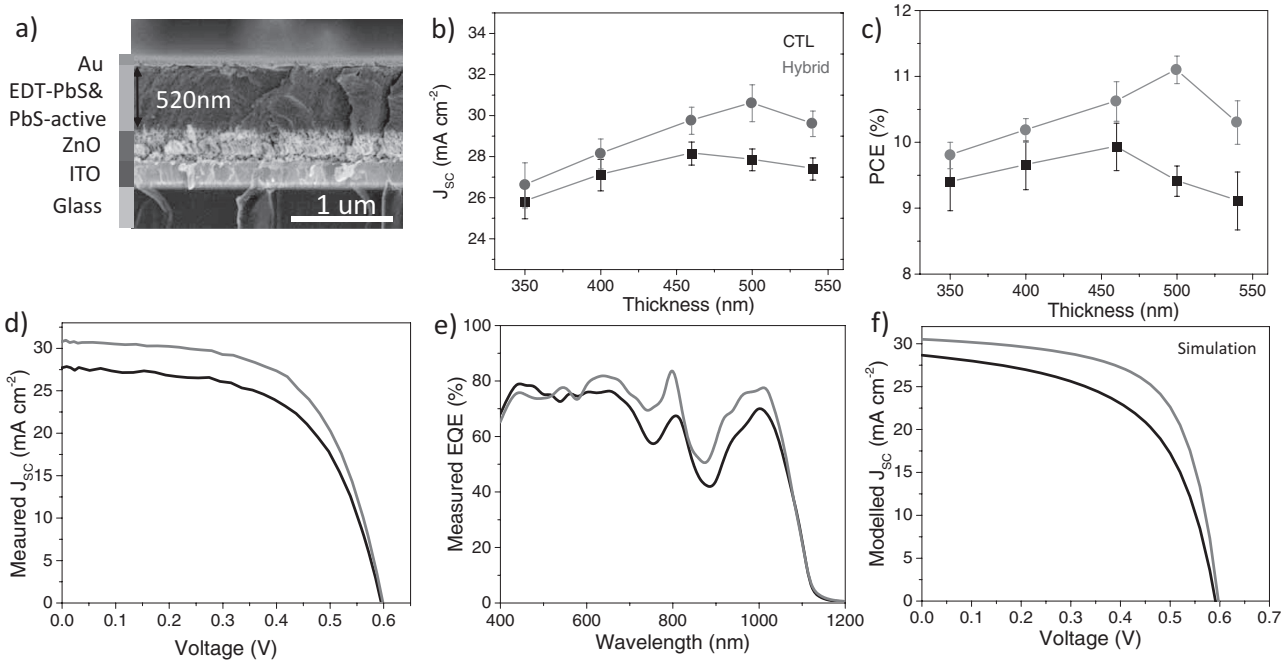

Figure 3. Device architecture and photovoltaic performance. a) Device architecture and cross-sectional SEM image of the best hybrid solar cell. b) Measured J_{SC} and c) PCE with different active layer thicknesses. d) *J–V* characteristics of optimal CTL and hybrid CQD solar cell devices. e) EQE curves of the CTL and hybrid devices. f) Simulated *J–V* curves of devices with varying trap densities.

the thickness-dependent J_{SC} and PCE for the CTL and hybrid devices (Figure 3b,c). J_{sc} increases with the thickness due to improved light absorption; it then diminishes when recombination losses through the thicker active layer begin to dominate. We obtained the best-performing hybrid devices when their active layer thickness reached 500 nm; whereas CTL devices showed an optimized thickness of ≈460 nm. We note that the hybrid devices achieve increased current and optimal thickness without loss to fill factor (FF) and V_{OC}. The optimal hybrid film produced a high J_{SC}, resulting in a PCE that reached 11.2%. No hysteresis was observed between forward and reverse scans (Figure S3, Supporting Information).

The V_{OC}, J_{SC}, and FF of the optimal hybrid devices are 0.60 V, 30.6 ± 0.9 mA cm^{-2}, and 59%, respectively. The best CTL device has a PCE as high as 9.8%, with the V_{OC}, J_{SC}, and FF at 0.59 V, 28 ± 0.8 mA cm^{-2}, and 58%, respectively. The histogram of device performance for optimal CTL and hybrid solar cells indicates that hybrid passivation improves photovoltaic performance systematically and statistically significantly (Figure S5, Supporting Information). The improvement in the hybrid devices mainly comes from the increase in J_{SC}. The increased J_{SC} for hybrid is consistent with the improved EQE over the spectral range 600–1100 nm seen in Figure 3e; the integrated J_{SC} values for hybrid and CTL devices are 30.4 and 27.8 mA cm^{-2}, respectively. The value of the EQE at the excitonic peak reached 80% in the case of hybrid device, significantly higher than that of the CTL device. This agrees with the interpretation that lowered trap density contributes to longer carrier diffusion lengths and thus enables efficient extraction from a thicker active layer. Simulation of the performance of optoelectronic devices predicts that a fourfold reduction of trap density improves J_{SC} of a photovoltaic device as shown in Figure 3f, which is in good agreement with the experimental results (details of experimental and computational techniques, see the Supporting Information).

In conclusion, the reduced trap density offered by the thiocyanate treatment provides the means to improve the diffusion length. We mapped the trap density of CQD films using FET spectroscopy, observing a trap density of 1.6×10^{16} cm^{-3}, a fourfold reduction relative to controls. The corresponding PCE reached 11.2%. Trap-assisted recombination was correspondingly reduced, a further step along the path to higher-performing CQD solar cells and light sensors.

Experimental Section

Materials and Characterization: The oleate-capped PbS CQDs and ZnO nanoparticles were synthesized following our previous reports. Other chemicals were obtained from commercial suppliers and used as is. The Fourier transform infrared (FTIR) spectroscopy measurements are done using a Bruker Vertex 80 (8000 to 600 cm^{-1}; resolution 4 cm^{-1}) in top-configuration (attenuated total reflection, ATR). Optical absorption measurements were performed on a Lambda 950 500 UV–Vis–IR spectrometer. PL measurements were carried out with a Horiba Fluorolog Time Correlated Single Photon Counting system equipped with UV/VIS/NIR photomultiplier tube detectors, dual grating spectrometers, and a monochromatized xenon lamp excitation source.

QDs Ligand Exchange and Solution Preparation: The PbX_2/AA DMF solution ligand exchange was carried out in a test tube in air. Precursor solution CTL (PbI_2 0.1 M and AA 0.04 M) and hybrid (PbI_2 0.095 M, $Pb(SCN)_2$ 0.005 M, and AA 0.04 M) are dissolved in DMF. 5 mL of oleate-capped PbS CQDs octane solution (10 mg mL^{-1}) were added to 5 mL of precursor solution, followed by vigorously mixing for 1–2 min until the CQDs completely transferred to the DMF phase. The DMF phase was then washed three times with octane. Then CQDs were precipitated by adding 3 mL of toluene and collected by centrifugation. After drying for 15 min, the CQDs were redispersed in butylamine (BTA) (200 mg mL^{-1}) for film by spin coating.

FET Fabrication: Bottom-gate top-contact FET configuration was used as follows: 70 nm of a titanium gate were thermally evaporated onto a glass substrate, followed by 10 nm of ZrO_2 as a dielectric layer using atomic layer deposition. After 300 °C baking for 1 h, pre-exchanged CQDs dissolved in BTA were spin-coated onto the substrate. Then 70 nm of Au source/drain electrodes were thermally deposited using an Angstrom Engineering Amod deposition system. Keithley 2400 source meters were used to characterize the FET devices.

Supporting Information

Supporting Information is available from the Wiley Online Library or from the author.

Acknowledgements

This publication is based in part on work supported by the Ontario Research Fund Research Excellence Program, and by the Natural Sciences and Engineering Research Council (NSERC) of Canada. H.T. acknowledges The Netherlands Organisation for Scientific Research (NWO) for a Rubicon grant (680-50-1511) in support of his postdoctoral research at the University of Toronto.

Conflict of Interest

The authors declare no conflict of interest.

Keywords

field-effect transistors, quantum dots, solar cells, surface passivation, thiocyanate

Received: February 6, 2017
Revised: March 23, 2017
Published online:

[1] C. B. Murray, C. R. Kagan, M. G. Bawendi, *Annu. Rev. Mater. Sci.* **2000**, *30*, 545.
[2] Y. I. Park, Y. Piao, N. Lee, B. Yoo, B. H. Kim, S. H. Choi, T. Hyeon, *J. Mater. Chem.* **2011**, *21*, 11472.
[3] W. W. Yu, Y. A. Wang, X. Peng, *Chem. Mater.* **2003**, *15*, 4300.
[4] C. B. Murray, D. J. Norris, M. G. Bawendi, *J. Am. Chem. Soc.* **1993**, *115*, 8706.
[5] E. H. Sargent, *Nat. Photonics* **2012**, *6*, 133.
[6] M. Yuan, M. Liu, E. H. Sargent, *Nat. Energy* **2016**, *1*, 16016.
[7] C. R. Kagan, C. B. Murray, *Nat. Nanotechnol.* **2015**, *10*, 1013.
[8] G. H. Carey, L. Levina, R. Comin, O. Voznyy, E. H. Sargent, *Adv. Mater.* **2015**, *27*, 3325.
[9] X. Lan, O. Voznyy, A. Kiani, F. P. G. de Arquer, A. S. Abbas, G.-H. Kim, M. Liu, Z. Yang, G. Walters, J. Xu, M. Yuan, Z. Ning, F. Fan, P. Kanjanaboos, I. Kramer, D. Zhitomirsky, P. Lee,

A. Perelgut, S. Hoogland, E. H. Sargent, *Adv. Mater.* **2016**, *28*, 299.
[10] H. Li, D. Zhitomirsky, S. Dave, J. C. Grossman, *ACS Nano* **2016**, *10*, 606.
[11] X. Lan, O. Voznyy, F. P. García de Arquer, M. Liu, J. Xu, A. H. Proppe, G. Walters, F. Fan, H. Tan, M. Liu, Z. Yang, S. Hoogland, E. H. Sargent, *Nano Lett.* **2016**, *16*, 4630.
[12] M. Liu, O. Voznyy, R. Sabatini, F. P. Garcia de Arquer, R. Munir, A. H. Balawi, X. Lan, F. Fan, G. Walters, A. R. Kirmani, S. Hoogland, F. Laquai, A. Amassian, E. H. Sargent, *Nat. Mater.* **2017**, *16*, 258.
[13] G. H. Carey, A. L. Abdelhady, Z. Ning, S. M. Thon, O. M. Bakr, E. H. Sargent, *Chem. Rev.* **2015**, *115*, 12732.
[14] J. Tang, E. H. Sargent, *Adv. Mater.* **2011**, *23*, 12.
[15] H. Choi, J.-H. Ko, Y.-H. Kim, S. Jeong, *J. Am. Chem. Soc.* **2013**, *135*, 5278.
[16] G. W. Hwang, D. Kim, J. M. Cordero, M. W. B. Wilson, C.-H. M. Chuang, J. C. Grossman, M. G. Bawendi, *Adv. Mater.* **2015**, *27*, 4481.
[17] J. Tang, K. W. Kemp, S. Hoogland, K. S. Jeong, H. Liu, L. Levina, M. Furukawa, X. Wang, R. Debnath, D. Cha, K. W. Chou, A. Fischer, A. Amassian, J. B. Asbury, E. H. Sargent, *Nat. Mater.* **2011**, *10*, 765.
[18] P. Stadler, B. R. Sutherland, Y. Ren, Z. Ning, A. Simchi, S. M. Thon, S. Hoogland, E. H. Sargent, *ACS Nano* **2013**, *7*, 5757.
[19] W. K. Bae, J. Joo, L. A. Padilha, J. Won, D. C. Lee, Q. Lin, W.-k. Koh, H. Luo, V. I. Klimov, J. M. Pietryga, *J. Am. Chem. Soc.* **2012**, *134*, 20160.
[20] Y. Gai, H. Peng, J. Li, *J. Phys. Chem. C* **2009**, *113*, 21506.
[21] A. H. Ip, S. M. Thon, S. Hoogland, O. Voznyy, D. Zhitomirsky, R. Debnath, L. Levina, L. R. Rollny, G. H. Carey, A. Fischer, K. W. Kemp, I. J. Kramer, Z. Ning, A. J. Labelle, K. W. Chou, A. Amassian, E. H. Sargent, *Nat. Nanotechnol.* **2012**, *7*, 577.
[22] J. Zhang, J. Gao, E. M. Miller, J. M. Luther, M. C. Beard, *ACS Nano* **2014**, *8*, 614.
[23] D. Zhitomirsky, O. Voznyy, L. Levina, S. Hoogland, K. W. Kemp, A. H. Ip, S. M. Thon, E. H. Sargent, *Nat. Commun.* **2014**, *5*, 3803.
[24] S. J. Oh, D. B. Straus, T. Zhao, J. H. Choi, S. W. Lee, E. A. Gaulding, C. B. Murray, C. R. Kagan, *Chem. Commun.* **2017**, *53*, 728.
[25] A. T. Fafarman, W.-k. Koh, B. T. Diroll, D. K. Kim, D.-K. Ko, S. J. Oh, X. Ye, V. Doan-Nguyen, M. R. Crump, D. C. Reifsnyder, C. B. Murray, C. R. Kagan, *J. Am. Chem. Soc.* **2011**, *133*, 15753.
[26] W.-k. Koh, S. R. Saudari, A. T. Fafarman, C. R. Kagan, C. B. Murray, *Nano Lett.* **2011**, *11*, 4764.
[27] H. Zhang, J. Jang, W. Liu, D. V. Talapin, *ACS Nano* **2014**, *8*, 7359.
[28] B. Hou, Y. Cho, B. S. Kim, J. Hong, J. B. Park, S. J. Ahn, J. I. Sohn, S. Cha, J. M. Kim, *ACS Energy Lett.* **2016**, *1*, 834.
[29] J. Gao, J. C. Johnson, *ACS Nano* **2012**, *6*, 3292.
[30] Z. Ning, O. Voznyy, J. Pan, S. Hoogland, V. Adinolfi, J. Xu, M. Li, A. R. Kirmani, J.-P. Sun, J. Minor, K. W. Kemp, H. Dong, L. Rollny, A. Labelle, G. Carey, B. Sutherland, I. Hill, A. Amassian, H. Liu, J. Tang, O. M. Bakr, E. H. Sargent, *Nat. Mater.* **2014**, *13*, 822.
[31] M. D. H. Chowdhury, P. Migliorato, J. Jang, *Appl. Phys. Lett.* **2013**, *103*, 152103.
[32] H.-C. Chu, Y.-S. Shen, C.-H. Hsieh, J.-H. Huang, Y.-H. Wu, *ACS Appl. Mater. Interfaces* **2015**, *7*, 15129.
[33] A. Rolland, J. Richard, J. P. Kleider, D. Mencaraglia, *J. Electrochem. Soc.* **1993**, *140*, 3679.

